Synthesis and Optical Spectroscopy of MnO_4^{2-}-Doped Crystals of Cs_2CrO_4, $SrCrO_4$, CsBr, and CsI

Ralph P. Schenker,[†] Thomas C. Brunold,[‡] and Hans U. Güdel*,[†]

Departement für Chemie, Universität Bern, Freiestrasse 3, CH-3000 Bern 9, Switzerland, and Department of Chemistry, Stanford University, Stanford, California 94305

Received August 8, 1997

The first low-temperature absorption and luminescence spectra of MnO_4^{2-}-doped crystals of Cs_2CrO_4, $SrCrO_4$, CsBr, and CsI are reported. Single crystals of Cs_2CrO_4:MnO_4^{2-}, which crystallize in the orthorhombic β-K_2SO_4 structure, were grown from basic aqueous solutions. An alkali−chloride flux composition was used to obtain single crystals of $SrCrO_4$:MnO_4^{2-} with the monoclinic monazite structure. Crystals of CsBr:MnO_4^{2-} and CsI:MnO_4^{2-} were prepared by slowly cooling the melt. The site symmetry in $SrCrO_4$ is C_1, but the deviations from D_2 symmetry are small, and the spectra are analyzed in the approximate D_2 symmetry. The $^2E \leftrightarrow {}^2T_2$ ligand-field transitions are strongly *c* polarized, and in absorption only the transition to the lowest-energy component of the split $^2T_2$ state is observed with its origin at 10 303 cm^{-1}. Luminescence is exclusively observed to the lower-energy component of the ^2E state. By a combination of absorption and luminescence data, it is shown that, in the cubic CsBr and CsI lattices, MnO_4^{2-} is partly incorporated in the form of Cs_2MnO_4 crystallites. The observed nonexponential luminescence decay for these systems indicates the existence of several manganese(VI) species with different relaxation times. Within isomorphous host lattices, a correlation is established between the temperature-quenching behavior and the size of the M^{6+} host ion: the efficiency of multiphonon relaxation processes increases with increasing ionic radius of M^{6+}.

1. Introduction

In MnO_4^{2-}, the Mn^{6+} ion, which is a $3d^1$ ion, is stabilized in a well-defined tetrahedral oxo-coordination. In the ^2E ground state, the single unpaired electron occupies the π antibonding set of e orbitals. In the first excited state, this electron is promoted to the π and σ antibonding set of t_2 orbitals, giving rise to the $^2T_2$ ligand-field (LF) excited state. The weak $^2E \rightarrow {}^2T_2$ LF absorption band is centered at about 12 500 cm^{-1} in the near-infrared (NIR). The lowest-energy $^2E \rightarrow {}^2T_2$ ligand-to-metal charge-transfer (LMCT) absorption band is centered at about 17000 cm^{-1} in the vis, causing the green color of MnO_4^{2-}.

The spectroscopic properties of MnO_4^{2-}-doped crystals were reported for various host lattices belonging to three different structure types: the orthorhombic β-K_2SO_4[1] and the $BaSO_4$[2] structures with space group *Pnma* and the cubic CsCl structure with space group *Pm*3*m*. Polarized low-temperature absorption spectra of MnO_4^{2-}-doped K_2CrO_4 and isomorphous alkali-metal sulfates[3,4] and $BaSO_4$[5] were published in the early 1970s. But the first luminescence spectra of MnO_4^{2-} doped into a variety of host lattices such as K_2MO_4 (M = S, Cr, Se), Cs_2SO_4, and $BaMO_4$ (M = S, Cr, Se) were reported only very recently.[6,7] From a thorough analysis of the absorption and luminescence spectra of MnO_4^{2-} in the Cs_2SO_4[8] and $BaSO_4$[9] hosts, a detailed picture of the electronic structure and vibronic interactions in the ^2E and $^2T_2$ LF states could be derived. Optical absorption, ESR, and Raman spectra of MnO_4^{2-} doped into CsBr[10] and CsI[11] and other alkali-metal halides[12] were reported; but a detailed analysis of their optical spectra is still lacking, likely due to the poorly resolved absorption spectra and the lack of luminescence spectra.

In this study we report the synthesis and optical spectroscopic properties of MnO_4^{2-}-doped crystals of Cs_2CrO_4, $SrCrO_4$, CsBr, and CsI, belonging to different structure types: Cs_2CrO_4 crystallizes in the β-K_2SO_4 structure, $SrCrO_4$ has a monoclinic crystal structure (space group $P2_1/n$, β = 103.08°) of the monazite type,[13] and CsBr and CsI crystallize in the cubic CsCl structure. On the basis of the low-temperature absorption, excitation, and luminescence spectra, the energy level schemes of MnO_4^{2-} in these host lattices are established and compared to those reported for the A_2MO_4 (A = K, Cs; M = S, Cr) and $BaMO_4$ (M = S, Se) hosts. Excited and ground state distortions along totally symmetric and Jahn−Teller coordinates are derived from the highly resolved luminescence spectrum of Cs_2CrO_4.

[†] Universität Bern.
[‡] Stanford University.

(1) Wyckoff, R. G. W. *Crystal Structures*, 2nd ed.; Interscience: New York, 1965; Vol. 3, p 95.
(2) Wyckoff, R. G. W. *Crystal Structures*, 2nd ed.; Interscience: New York, 1965; Vol. 3, p 45.
(3) Day, P.; DiSipio, L.; Ingletto, G.; Oleari, L. *J. Chem. Soc., Dalton Trans.* **1973**, 2595.
(4) DiSipio, L.; Oleari, L.; Day, P. *J. Chem. Soc., Faraday Trans. 2* **1972**, *68*, 1032.
(5) Kosky, C. A.; McGarvey, B. R.; Holt, S. L. *J. Chem. Phys.* **1972**, *56*, 5904.
(6) Brunold, T. C.; Hazenkamp, M. F.; Güdel, H. U. *J. Am. Chem. Soc.* **1995**, *117*, 5598.
(7) Brunold, T. C.; Güdel, H. U. *Chem. Phys. Lett.* **1996**, *249*, 77.
(8) Brunold, T. C.; Güdel, H. U.; Riley, M. J. *J. Chem. Phys.* **1996**, *105 (18)*, 7931.
(9) Brunold, T. C.; Güdel, H. U. *Inorg. Chem.* **1997**, *36*, 1946.
(10) Radhakrishna, S.; Hariharan, K. *Phys. Status Solidi B* **1979**, *92*, 293.
(11) Martin, T. P.; Onari, S. *Phys. Rev. B* **1977**, *15*, 1093.
(12) Jain, S. C.; Agarwal, S. K.; Sootha, G. D. *J. Phys. Chem. Solids* **1971**, *32*, 897.
(13) Effenberger, H.; Pertlik, F. *Z. Kristallogr.* **1986**, *176*, 75.

S0020-1669(97)01004-5 CCC: $15.00
Published on Web 02/10/1998

Differences in the luminescence band shapes, lifetimes, and quantum yields among the various host lattices are analyzed. A correlation is established between the luminescence quenching behavior and the size of the M^{6+} ion for which Mn^{6+} substitutes in the host lattice. By chemical and structural variation of the host lattice, the spectroscopic processes can be significantly influenced.

2. Experimental Section

2.1. Synthesis. All the chemicals used for the present study were of analytical grade except $CsOH \cdot H_2O$ (<5% Cs_2CO_3).

Cs_2CrO_4:MnO_4^{2-}. Single crystals of Cs_2CrO_4:MnO_4^{2-} were grown from a strong basic aqueous solution of MnO_4^{2-} saturated with Cs_2CrO_4 using the temperature-difference method described in ref 14. After dissolving in 6 M CsOH, $KMnO_4$ is rapidly reduced to MnO_4^{2-} by OH^-.[15] The solutions were initially 2.5×10^{-4} M in MnO_4^{2-} to grow crystals for absorption experiments in the vis and the luminescence measurements and 2.5×10^{-3} M for the crystals to measure the weak d → d absorption in the NIR. After saturation with Cs_2CrO_4, the solutions were transferred into the crystal growth tubes.[14] Crystals of green color and of high optical quality were obtained within 15−30 days. The rhombohedrally shaped crystals were found to be elongated along their crystallographic *b* axis by X-ray diffraction. Samples for optical absorption measurements were obtained by polishing the deep green crystals to thin disks parallel to the crystallographic (001) plane for measurements in *a* and *b* polarizations and parallel to the (010) plane for measurements in *a* and *c* polarizations.

$SrCrO_4$:MnO_4^{2-}. Because of the insolubility in water and the high melting point of the host material, single crystals of $SrCrO_4$:MnO_4^{2-} were prepared using the flux method. Manganese was added to $SrCrO_4$ as $KMnO_4$, which is reduced to MnO_4^{2-} above 220 °C in air. To prevent the formation of MnO_4^{2-},[16] the growth temperature must be kept below 620 °C. We used a ternary flux system composed of NaCl, KCl, and CsCl, in analogy to the synthesis of $BaSO_4$:MnO_4^{2-}.[9] Best results were obtained with the molar composition NaCl (24.8%), KCl (26.4%), CsCl (41.3%), and $SrCrO_4$ (7.5%). The amount of $KMnO_4$ was varied in several attempts between 0.8 and 5 mol % with respect to $SrCrO_4$. The starting materials were thoroughly mixed, placed in a platinum crucible with a tight-fitting lid, and kept for 12 h at 620 °C in a temperature-controlled furnace. The mixture was slowly cooled first to 530 °C at −1.5 °C/h, then to 450 °C at −2 °C/h, and finally to room temperature at −50 °C/h. Due to the low solubility of $SrCrO_4$, the crystals could be separated from the flux by washing the cake in water. The crystals obtained were always yellow. Only a very small fraction of the MnO_4^{2-} originally present in the melt was incorporated into the host lattice. Some crystals were of a well-defined flat shape and therefore suitable for spectroscopic measurements. The single crystal used for the present studies was $1.7 \times 1.6 \times 0.95$ mm^3 with a well-defined crystal face identified as the crystallographic $(2\bar{1}0)$ plane. Its MnO_4^{2-} concentration was found to be 45 ppm by measuring the absorption spectrum in the vis.

CsBr:MnO_4^{2-} and CsI:MnO_4^{2-}. Crystals of CsBr and CsI doped with MnO_4^{2-} were prepared by slowly cooling the melts. Manganese was introduced as $MnCl_2 \cdot 4H_2O$, which is oxidized by air oxygen to MnO_4^{2-} in the presence of Cs_2CO_3 during the heating process.[17] Best results were obtained using the following procedure: A 4.00 g sample (18.8 mmol) of CsBr was mixed with 7.5 mg (38 μmol) of $MnCl_2 \cdot 4H_2O$, corresponding to an initial manganese concentration of 0.2 mol %. Then 36.8 mg (0.133 mmol) of Cs_2CO_3 was added, and the substances were thoroughly mixed and transferred to a quartz glass ampule. The open ampule was heated to 670 °C in a temperature-controlled furnace for 30 min, slowly cooled to 520 °C at −10 °C/h, and then cooled to room temperature at −50 °C/h. Pale blue-turquoise crystals with an ill-defined shape were obtained. They appeared to be single-crystalline, but under the microscope needlelike and blue inclusions up to 25 μm in length were observed. Outside the inclusions, the crystals appeared essentially colorless. Traces of MnO_2 were found outside the crystal boule in the ampule. The volume of the crystals was typically 1−8 mm^3. For absorption experiments, a crystal of 2.5 × 2.0 × 0.8 mm^3 was polished to obtain two parallel faces. Crystals of CsI:MnO_4^{2-} were grown using a similar procedure.

Cs_2MnO_4. To simulate the postulated domains of Cs_2MnO_4 in CsBr and CsI (see section 4.1), mixtures of Cs_2MnO_4 and CsCl powders were pressed into pellets. Cs_2MnO_4 was prepared according to a literature procedure.[18] The product was characterized by X-ray powder diffraction and used without further purification. The amounts of Cs_2MnO_4 in the pellets were 0.1, 1, and 10 mol % with respect to CsCl. Samples of pure Cs_2MnO_4 were also prepared. The substances were thoroughly ground in a mortar and then pressed into pellets for 20 min at a pressure of 10 bar.

2.2. Spectroscopic Measurements. Single-crystal absorption spectra in the vis and UV spectral regions were recorded on a double-beam spectrometer (Cary 05e) fitted with a closed-cycle helium refrigerator (Air Products) for sample cooling to 15 K. High-resolution absorption spectra in the NIR region were measured on a home-built double-beam spectrometer based on a double monochromator (Spex 1402) and equipped with a red-sensitive PM tube (Hamamatsu R 406). The samples were cooled to 20 K in a cold helium-gas stream using the flow tube technique.

Broad-band excitation of the luminescence was performed with a xenon lamp (Osram XBO 150 W/1) filtered by a saturated aqueous Cu^{2+} solution and a color filter (Schott KG 4). The emitted light was dispersed by a single monochromator (3/4 m Spex 1701), equipped with a grating blazed at 1.25 μm, and detected by a germanium detector (ADC 403 L, cooled to 77 K) in combination with a lock-in amplifier (SR 510 or SR 830). The spectra were corrected for system response and show the number of photons per unit energy and unit time. For time-dependent measurements the samples were excited at 532 nm with the second harmonic of a pulsed YAG:Nd laser (Quanta-Ray DCR-3). The emitted photons were detected with a cooled PM tube (Hamamatsu R 3310). Luminescence decay curves were recorded with a multichannel scaler (SR 430) at 980 nm. Excitation spectra were obtained using the sample beam of the double-beam instrument. The emitted light was filtered by a Si filter and recorded in the same way as described for the luminescence measurements. Variable sample temperatures between 10 and 300 K were achieved with a cold helium-gas flow technique.

3. Results

3.1. Absorption and Excitation Spectra. The polarized 20 K absorption spectra of Cs_2CrO_4:MnO_4^{2-} for *E* parallel to *a* and *b* are shown in Figure 1, broken and solid lines, respectively. In the near-infrared (NIR), a weak band system extends from 10 466 cm^{-1} (origin) to about 14 500 cm^{-1} and exhibits a well-resolved fine structure in *b* polarization. From a comparison with the absorption spectra of Cs_2SO_4:MnO_4^{2-},[8] it is assigned to the $^2E \rightarrow {}^2T_2$ ligand-field (LF) transition of MnO_4^{2-}. A much stronger absorption band is observed between 16 000 and 20 000 cm^{-1}. It is readily assigned to the lowest energy $^2E \rightarrow {}^2T_2$ ligand-to-metal charge-transfer (LMCT) transition.[8] In both polarizations it shows a well-resolved vibrational progression in the totally symmetric Mn−O stretching (*ν*) mode. For $E||b$ the vibrational sidebands are split into two components. The intensity ratios of the two partners in each pair vary along the progression, indicating the presence of two overlapping band systems in this polarization. Their respective origins are at 16 008 and 16 099 cm^{-1}. In *a* polarization, there is a single band system with an origin at 16 073 cm^{-1}. In this polarization,

(14) Hulliger, J. *Angew. Chem.* **1994**, *106*, 162.
(15) *Gmelins Handbuch der anorganischen Chemie*; Springer: Berlin, 1975; Vol. 56, Mn (C2), p 52.
(16) Booth, J. S.; Dollimore, D.; Heal, G. R. *Thermochim. Acta* **1980**, *39*, 281.
(17) Meller, J. W. *Comprehensive Treatise on Inorganic and Theoretical Chemistry*; Longmans Green: New York, 1947; Vol. 12, p 281.
(18) Nyholm, R. S.; Woolliams, P. R. *Inorg. Synth.* **1968**, *11*, 56.

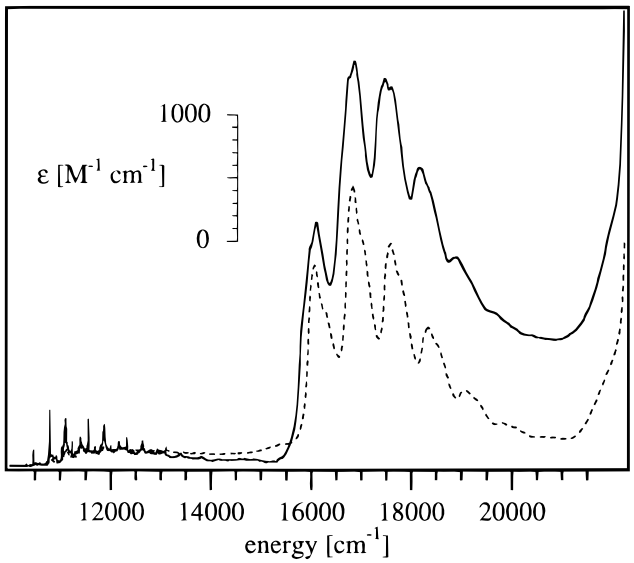

Figure 1. *E*||*b* (solid line) and *E*||*a* (broken line) polarized 20 K absorption spectra of Cs_2CrO_4:MnO_4^{2-} in the vis and NIR regions.

Table 1. Origin Positions, Vibrational Frequencies (cm^{-1}), and Huang−Rhys Parameters *S* for the Progression in the Mn−O Stretching (ν) Mode for the Lowest-Energy $^2E \rightarrow {}^2T_2$ LMCT Transition of MnO_4^{2-} in Various Host Lattices[a]

host	polarizn	origin	ν	*S*
Cs_2SO_4	*E*||*b*, #1	16 138	750	1.7
	E||*b*, #2	16 349	755	1.6
	E⊥*b*	16 229	773	1.4
Cs_2CrO_4	*E*||*b*, #1	16 008	740	1.8
	E||*b*, #2	16 099	760	1.7
	E⊥*b*	16 073	757	1.5
$BaSO_4$	*E*||*a*	17 266	730	1.7
	E||*b*	16 868	795	1.5
$BaSeO_4$	*E*||*a*	16 750	730	
	E||*b*	16 530	793	
$SrCrO_4$	*E*||*c*	15 452	757	1.6
	E⊥*c*	15 380	758	
CsBr		16 151	760	1.5
CsI		16 125	730	1.5

[a] For Cs_2SO_4 and Cs_2CrO_4, the two origins observed in *b* polarization are designated by #1 and #2.

each member of the progression in the ν mode carries a shoulder on its high-energy side corresponding to the first sideband of a progression in the O−Mn−O bending (δ) mode of 209 cm^{-1}. Above 21 500 cm^{-1}, the strong increase in absorption is due to the onset of the host absorption.[19] The absorption spectra in the 15 000−20 000 cm^{-1} region of MnO_4^{2-} doped into $SrCrO_4$, CsBr and CsI are not shown; they are similar to the spectra in Figure 1. But the vibrational structure is less resolved. In the case of $SrCrO_4$:MnO_4^{2-}, the absorption between 15 000 and 20 000 cm^{-1} is predominantly *c* polarized. The spectra of CsBr:MnO_4^{2-} and CsI:MnO_4^{2-} are very similar to each other. Origin positions and vibrational frequencies for the progression in the ν mode for the lowest-energy $^2E \rightarrow {}^2T_2$ LMCT transition of MnO_4^{2-} in different host lattices are listed in Table 1.

Figure 2 shows the *E*||*a*, *E*||*b*, and *E*||*c* polarized 20 K absorption spectra of Cs_2CrO_4:MnO_4^{2-} in the region of the $^2E \rightarrow {}^2T_2$ LF transition in detail. They consist of a predominantly *E*||*b* polarized broad band system exhibiting a well-resolved vibrational structure built on the origin at 10 466 cm^{-1} (labeled I in *b* polarization). This dominant band system is superimposed

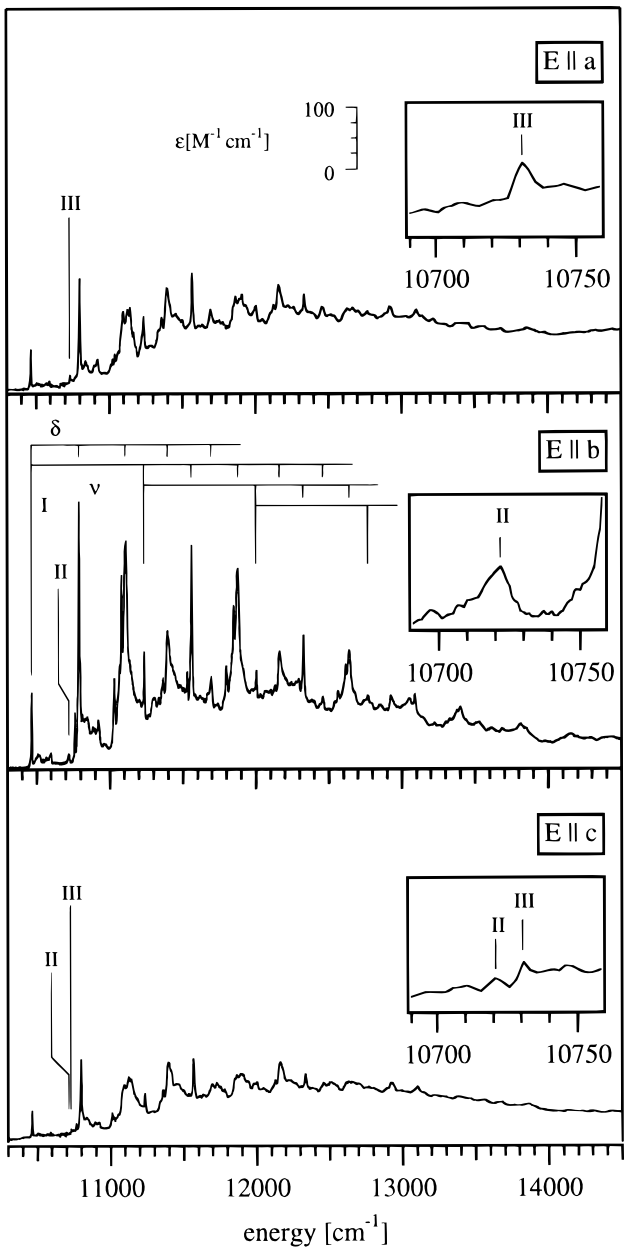

Figure 2. *E*||*a*, *E*||*b*, and *E*||*c* polarized $^2E \rightarrow {}^2T_2$ (LF) absorption spectra of Cs_2CrO_4:MnO_4^{2-} in the NIR region at 20 K. Three electronic origins (I, II, and III) are indicated. Progressions in the bending (δ) and stretching (ν) modes and their combination bands are assigned for transition I in the *E*||*b* spectrum. The regions of origins II and III are shown in the small insets on an expanded scale. The scale of the ordinate is the same in all three spectra.

by two much weaker systems. The origin of the second band system is located at 10 722 cm^{-1} (labeled II) and appears exclusively in *b* and *c* polarizations. The third band system has its origin at 10 731 cm^{-1} (labeled III) and is *a* and *c* polarized. The region of the origin lines II and III is shown in the small insets on an expanded scale in Figure 2. The three origin positions and the vibrational sidebands for the progressions in the totally symmetric Mn−O stretching (ν) and O−Mn−O bending (δ) modes built on origin I in *E*||*b* polarization are indicated at the top of the spectrum. The dominant progression-forming mode is the bending mode, whereas coupling to the stretching mode is less important. This is reflected by the Huang−Rhys parameters *S*, which are substantially larger for the bending mode than for the stretching mode; see Table 2. *S* is defined by the intensity ratio of the

(19) Ballhausen, C. J.; Liehr, A. D. *J. Mol. Spectrosc.* **1958**, *2*, 342.

Table 2. Origin Positions and Vibrational Frequencies (cm^{-1}) Together with the Respective Huang−Rhys Parameters *S* for the Progression-Forming O−Mn−O Bending (δ) and the Mn−O Stretching (ν) Modes for the $^2E \rightarrow {}^2T_2$ LF Absorption of MnO_4^{2-} in Various Host Lattices[a]

host	transn	origin	ν	$S(\nu)$	δ	$S(\delta)$
Cs_2CrO_4	I	10 466	770	0.66*	325	3.51*
	II	10 722	769		308	
	III	10 731	770	0.49	307	
$SrCrO_4$	I	10 303	785	0.32*	382	2.45*
CsBr	I	10 440	760		335	
CsI	I	10 425	760		330	

[a] Huang−Rhys parameters marked with an asterisk were obtained by fitting a simulated band shape to the experimental spectrum.[9] Transitions I, II, and III are explained in the text.

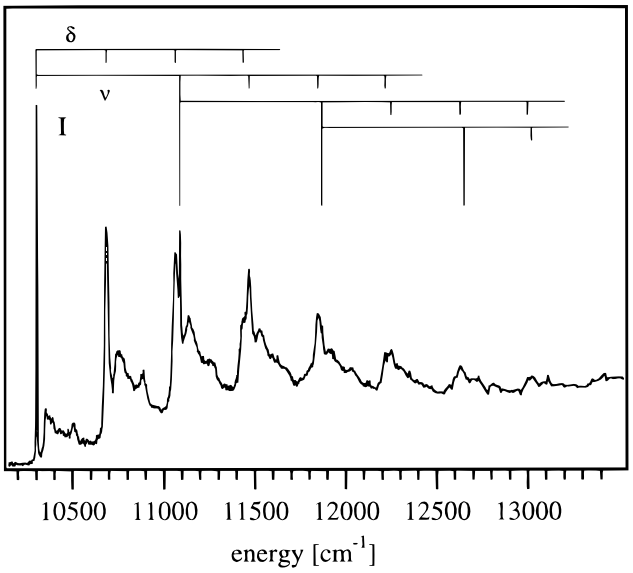

Figure 3. Unpolarized 20 K $^2E \rightarrow {}^2T_2$ (LF) excitation spectrum of $SrCrO_4$:MnO_4^{2-} in the NIR region. Origin I and the corresponding progressions in the bending (δ) and stretching (ν) modes are indicated. The excitation spectrum was obtained by detecting the luminescence below 10 000 cm^{-1}.

first sideband to the respective origin line. The determination of *S* for transitions II and III is made difficult by the dominance of the superimposed sidebands of system I.

The unpolarized 20 K luminescence excitation spectrum of $SrCrO_4$:MnO_4^{2-} in the region of the $^2E \rightarrow {}^2T_2$ (LF) transition is shown in Figure 3. The excitation spectrum was obtained by detecting the luminescence below 10 000 cm^{-1}. It consists of a higly structured broad-band system with an origin at 10 303 cm^{-1}. In analogy to Cs_2CrO_4:MnO_4^{2-}, the sideband structure is dominated by progressions in the bending (δ) mode, whereas coupling to the stretching (ν) mode is less pronounced. Polarized absorption spectra in the corresponding region (not shown) demonstrate that this transition is essentially $E||c$ polarized.

Figure 4 shows the 20 K excitation and absorption spectra of MnO_4^{2-} doped into CsBr in the region of the $^2E \rightarrow {}^2T_2$ (LF) transition. The excitation spectrum was obtained by detecting the luminescence below 10 000 cm^{-1}. It shows a fairly resolved band system with its origin at 10 436 cm^{-1} (labeled I). Apart from the larger line widths, it is similar to the $E||b$ polarized absorption spectrum of Cs_2CrO_4:MnO_4^{2-} shown in Figure 2. Both the vibrational frequencies of the progression-forming modes and the positions of origin I are very similar; see Table 2. The absorption spectrum shown at the bottom of Figure 4 has the same band positions as the excitation spectrum. The

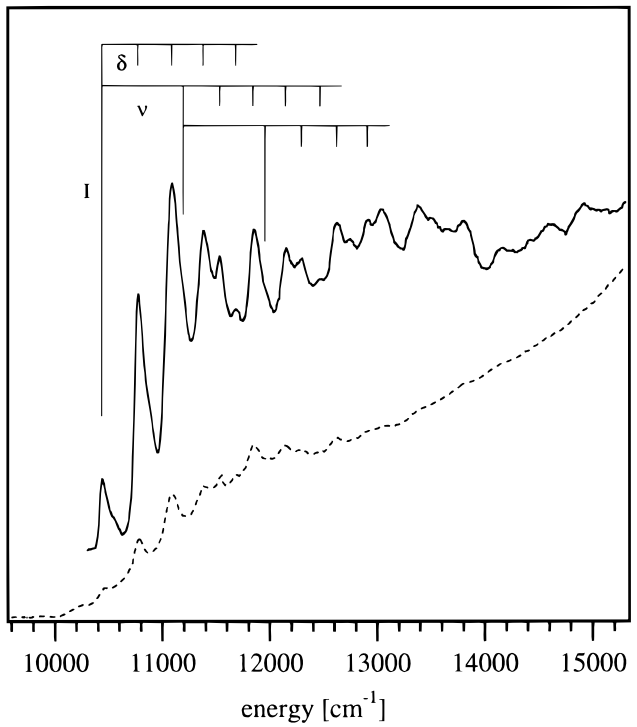

Figure 4. Excitation (solid line) and absorption (broken line) spectra of the $^2E \rightarrow {}^2T_2$ (LF) transition of CsBr:MnO_4^{2-} in the NIR region at 20 K. Origin I and the respective progressions in the bending (δ) and stretching (ν) modes are indicated. The excitation spectrum was obtained by detecting the luminescence below 10 000 cm^{-1}.

corresponding spectra of MnO_4^{2-}-doped CsI (not shown) are very similar to those of the bromide.

The origin positions and vibrational energies for the progressions in the stretching (ν) and bending (δ) modes together with the respective Huang−Rhys parameters *S* for the $^2E \rightarrow {}^2T_2$ LF transition of MnO_4^{2-} in the host lattices used for the present study are listed in Table 2. In those cases where sideband splitting or strong coupling of the electronic transition to lattice vibrations occur, the values of *S* were obtained by fitting a simulated band shape to the respective experimental spectrum using the procedure described in ref 9. Huang−Rhys parameters obtained in this way are marked with an asterisk in the table.

3.2. Emission Spectra. The unpolarized 15 K luminescence spectrum of Cs_2CrO_4:MnO_4^{2-} is shown in Figure 5, lower graph. It consists of two unusually well-resolved overlapping broad-band systems. The two electronic origins denoted by *I* and *J* are located at 10 466 and 9506 cm^{-1}, respectively. From the coincidence of origin *I* with origin I in absorption, the emission band is assigned to the $^2T_2 \rightarrow {}^2E$ transition of MnO_4^{2-}. As in absorption, the main progression-forming mode is the bending (δ) mode, whereas coupling to the stretching (ν) mode is less important. The sidebands in the bending-mode progression show slightly irregular spacings, and some of the lines are split. These are clear indications of a Jahn−Teller effect, as will be analyzed and discussed in section 4.1.1.

The upper graph of Figure 5 shows the unpolarized $^2T_2 \rightarrow {}^2E$ luminescence spectrum of $SrCrO_4$:MnO_4^{2-} at 15 K. Due to a stronger coupling of the electronic transition to lattice vibrations in this system than in Cs_2CrO_4:MnO_4^{2-}, the sharp lines are accompanied by phonon sidebands of higher intensity, thus washing out the sharp features at lower energies. There is a single broad-band system built on origin *I* at 10 303 cm^{-1}. The progressions in the stretching (ν) and bending (δ) modes are indicated at the top of the spectrum. Similar to those of

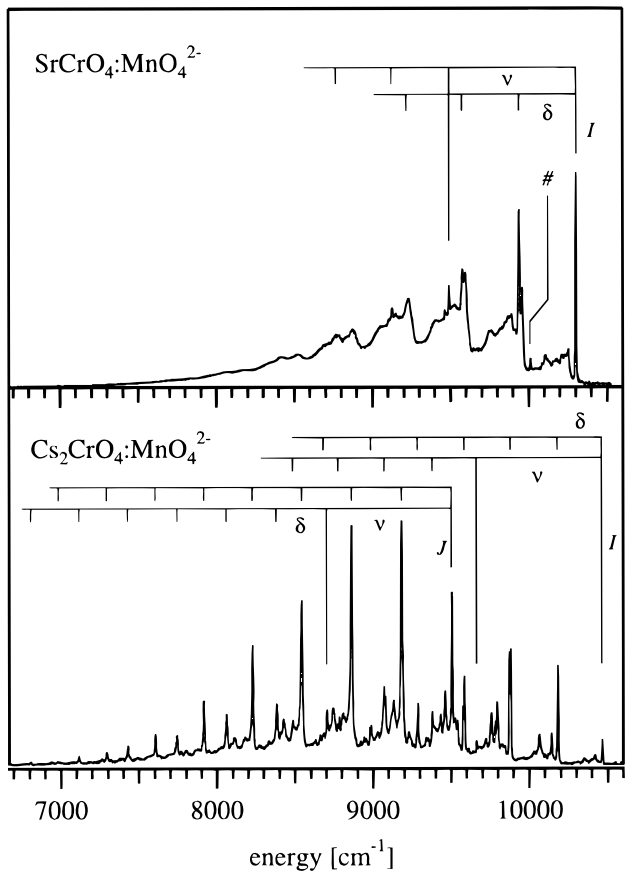

Figure 5. Unpolarized $^2T_2 \rightarrow {}^2E$ luminescence spectra of MnO_4^{2-} doped into $SrCrO_4$ (upper curve) and Cs_2CrO_4 (lower curve) at 15 K. In the case of $SrCrO_4:MnO_4^{2-}$, a single origin (I) and the respective progressions in the bending (δ) and stretching (ν) modes are indicated. The sharp line at 10 013 cm^{-1} (labeled #) is assigned as one quantum of the t_2 bending mode of MnO_4^{2-} built on origin *I*. In the spectrum of $Cs_2CrO_4:MnO_4^{2-}$, two electronic origins (*I* and *J*) and their respective progressions in the bending (δ) and stretching (ν) modes are indicated.

$Cs_2CrO_4:MnO_4^{2-}$, the progressions in the bending (δ) mode are dominant, and some of the sidebands are split. There is a weak line at 10 013 cm^{-1} denoted by # in Figure 5. On the basis of its separation of 290 cm^{-1} from origin I, we assign it to a totally symmetric component of the bending mode transforming as t_2 in the parent T_d symmetry.

A comparison of the emission spectra of $SrCrO_4:MnO_4^{2-}$ and $Cs_2CrO_4:MnO_4^{2-}$ in Figure 5 shows that the relative luminescence intensities of the band systems built on origins *I* and *J* are very different: While for $SrCrO_4:MnO_4^{2-}$ all the intensity is contained in the single band system *I*, the band system *J* is stronger than *I* in the case of $Cs_2CrO_4:MnO_4^{2-}$. Polarized luminescence measurements on $SrCrO_4:MnO_4^{2-}$ (not shown) reveal a strong polarization dependence of the whole band system: The intensity ratio $E||c/E\perp c$ is 5/1.

The upper, intermediate, and lower graphs of Figure 6 show the unpolarized 20 K luminescence spectra of $CsCl:Cs_2MnO_4$ and of MnO_4^{2-} doped into CsBr and CsI, respectively. Except for the decreasing resolution, the three spectra are very similar, and they are also very similar to the emission spectrum of pure Cs_2MnO_4. The spectra are similar to the corresponding spectrum of $Cs_2CrO_4:MnO_4^{2-}$ (see Figure 5). There are two overlapping band systems built on origins *I* and *J*, respectively. Again, the main progression-forming mode is the bending (δ) mode, whereas coupling to the stretching (ν) mode is less important. The positions of the origins and the energies of the

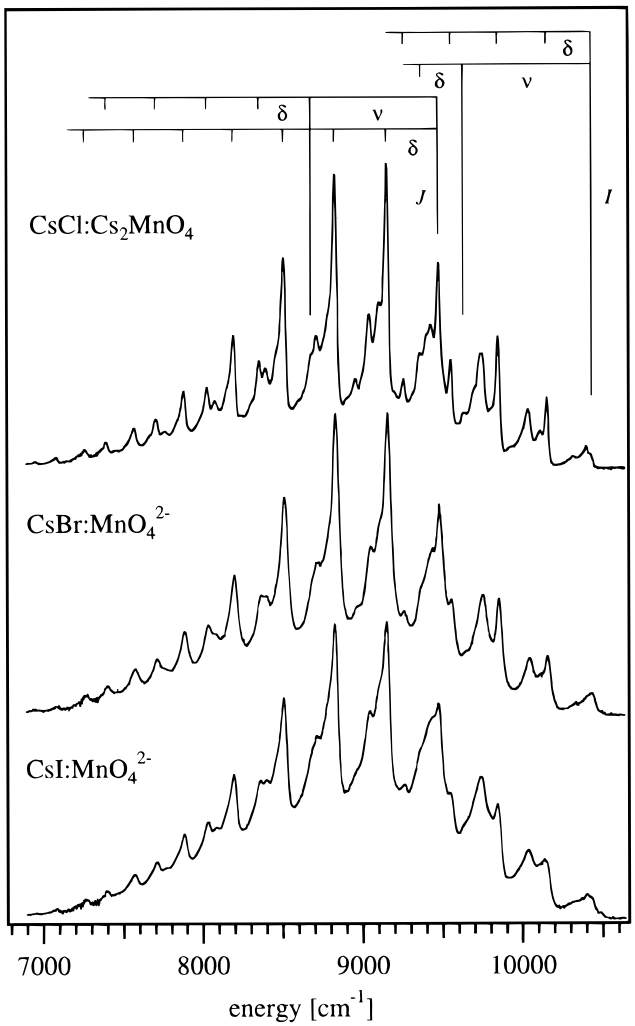

Figure 6. Unpolarized $^2T_2 \rightarrow {}^2E$ luminescence spectra of $CsCl:Cs_2MnO_4$, $CsBr:MnO_4^{2-}$, and $CsI:MnO_4^{2-}$ at 20 K. The progressions in the bending (δ) and stretching (ν) modes are indicated.

Table 3. Origin Positions and Vibrational Frequencies (cm^{-1}) Together with the Respective Huang−Rhys Parameters *S* for the Progression-Forming O−Mn−O Bending (δ) and the Mn−O Stretching (ν) Modes for the $^2T_2 \rightarrow {}^2E$ Luminescence of MnO_4^{2-} in Various Host Lattices[a]

host	transn	origin	ν	$S(\nu)$	δ(e)	$S(\delta)$	$\delta(t_2)$	Δ
Cs_2CrO_4	*I*	10 466	802	0.34	299	2.9	402	960
	J	9 506	799	0.12	323	2.42*		
$SrCrO_4$	*I*	10 303	811	0.25*	360	2.53*	290	(567)
	J							
$CsCl:Cs_2MnO_4$	*I*	10 435	794		306		396	957
	J	9 478	798		325			
CsBr	*I*	10 440	788		305		394	959
	J	9 481	786		325			
CsI	*I*	10 425	779		295		390	950
	J	9 475	780		324			

[a] Huang−Rhys parameters marked with an asterisk were obtained by fitting a simulated band shape to the experimental spectrum.[9] The energy difference Δ between origins *I* and *J* observed in the corresponding luminescence spectra is given in the last column. The value listed for $SrCrO_4$ was obtained from an AOM calculation.

δ and ν progressions are given in Table 3. They are very similar indeed, with a very slight trend to lower values along the series.

The luminescence decay times at 10 K of MnO_4^{2-} doped into a variety of host lattices are collected in Table 4. With the exception of those of the halides, they all lie within the range 1.5−3 μs. For the halides, the decay is nonexponential

Table 4. Luminescence Decay Times τ_{obs} at 10 K (μs) and $T_{10\%}$ Values (K) in Several Host Lattices[a]

host	τ_{obs}(10 K)	$T_{10\%}$	c, mol %	J, cm^{-1}
K_2SO_4	2.32	213	0.1	9833
K_2CrO_4	2.19	193	0.1	9670
Cs_2SO_4	1.72	285	0.1	9589
Cs_2CrO_4	1.65	271	0.1	9506
$SrCrO_4$	2.51	230	0.0045	
$BaSO_4$	2.75	350	0.1	~10700
$BaSeO_4$	2.21	285	0.1	~10320
$CsCl:Cs_2MnO_4$	(1.0)	158	0.1	9478
CsBr	(1.23)	164	0.2	9481
CsI	(1.24)	147	0.05	9475

[a] The $T_{10\%}$ value is defined as the temperature at which the luminescence intensity is reduced to 10% of its 10 K value. In the case of $CsCl:Cs_2MnO_4$, CsBr, and CsI, the τ_{obs} values were obtained from fits to the tail of the decay curves, giving an upper limit for τ_{obs}. The fourth column gives the nominal concentrations of MnO_4^{2-}, except for $SrCrO_4$, where the experimentally determined actual value is given. The last column lists the energies of the origin J in luminescence, corresponding to the smallest energy gap between excited and ground states.

with lifetimes of the longest-lived species of about 1 μs. Also included in Table 4 are the so-called $T_{10\%}$ values. These are the temperatures at which the luminescence intensity has dropped to 10% of its 10 K value. Except for those of the halides, these "quenching temperatures" range from 193 K for K_2CrO_4 to 350 K for $BaSO_4$. For the halides there is substantial quenching of the luminescence below 160 K. Pure Cs_2MnO_4 was found to have the same luminescence decay and quenching behavior as Cs_2MnO_4 finely dispersed in a CsCl pellet.

4. Discussion

4.1. $^2E \leftrightarrow {}^2T_2$ Ligand-Field Transitions. 4.1.1. Cs_2CrO_4 Host Lattice. Since Cs_2CrO_4 is isostructural with Cs_2SO_4, similar spectroscopic properties of MnO_4^{2-} doped into the two hosts are expected, and the spectra of $Cs_2CrO_4:MnO_4^{2-}$ can be analyzed in analogy to those of $Cs_2SO_4:MnO_4^{2-}$. Therefore we do not provide a detailed analysis of the optical spectra of $Cs_2CrO_4:MnO_4^{2-}$ here but rather refer to ref 8 and give a summary of the results.

The only symmetry element of the CrO_4^{2-} ion in Cs_2CrO_4 is a mirror plane (σ) perpendicular to the crystallographic b axis, and the site symmetry is thus C_s.[20] Adopting the axis orientation from ref 8, the molecular x axis coincides with b, and the y and z axes lie in the ac mirror plane with a rotation of 37° from the a and c axes, respectively. The effect of the $T_d \rightarrow C_s$ distortion on the $^2E \leftrightarrow {}^2T_2$ LF transitions of MnO_4^{2-} is illustrated in the right-hand side of Figure 7.[8] Spin−orbit coupling is neglected because its effect on band splittings is largely quenched by the crystal field. Both the ground and excited LF states split into their orbital components. In C_s, the components of the electric-dipole (ed) operator along x, y, and z transform as A″, A′, and A′, respectively. This gives rise to the selection rules shown by arrows in Figure 7: solid and dashed−dotted lines correspond to x- and y,z-polarized transitions, respectively.

The three electronic origins for the $^2E \rightarrow {}^2T_2$ LF transition of MnO_4^{2-} indicated in the absorption spectra of Figure 2 are assigned to the orbital components of $^2T_2$ on the basis of the selection rules sketched in Figure 7. The predominantly b polarized absorption I is assigned to the $^2A''(xy) \rightarrow {}^2A'(yz)$ transition. Absorption II, which corresponds to $^2A''(xy) \rightarrow {}^2A'$-$(x^2 - y^2)$, is observed in both b and c polarizations. Absorption III is due to $^2A''(xy) \rightarrow {}^2A''(xz)$ and appears in a and c polarizations. We ascribe this partial relaxation of the selection rules to spin−orbit coupling.

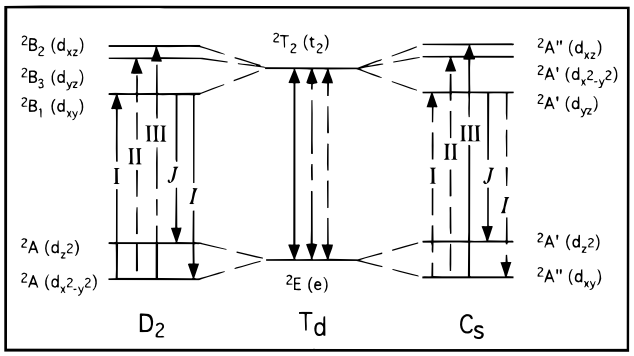

Figure 7. $T_d \rightarrow C_s$ and $T_d \rightarrow D_2$ splittings of the ligand-field (LF) states of MnO_4^{2-} in Cs_2CrO_4 and $SrCrO_4$, respectively. Electric-dipole-allowed transitions are shown by arrows; short-dashed, long-dashed, and solid lines correspond to x-, y-, and z-polarized transitions, respectively. In the case of $Cs_2CrO_4:MnO_4^{2-}$ (C_s), transitions III and J are both y and z polarized. The designation of the absorptions I, II, and III and emissions I and J relates to Figures 3−7.

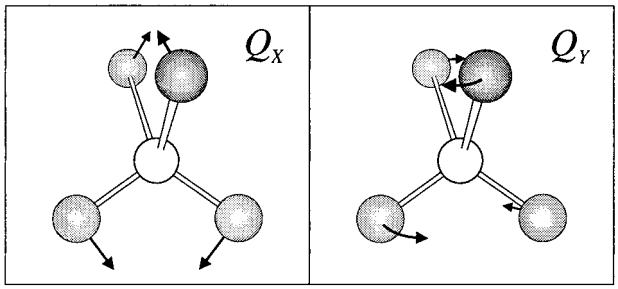

Figure 8. Illustration of the two components (Q_X and Q_Y) of the e bending mode in a tetrahedral MO_4 complex.

As shown in ref 8, the $T_d \rightarrow C_s$ distortion is moderate, and the splitting of the LF states is thus expected to be small. However, the luminescence spectrum shows a large value of the ^2E ground-state splitting for $Cs_2CrO_4:MnO_4^{2-}$ of 960 cm^{-1} (see Table 3). This is due to the effect of the poorly shielded positive charges of the Cs^+ ions creating a substantial crystal-field potential at the MnO_4^{2-} site.

Both the absorption (Figure 2) and luminescence (Figure 5) spectra demonstrate that coupling of the totally symmetric stretching (ν) mode to the $^2E \leftrightarrow {}^2T_2$ LF transitions is weak; see the corresponding Huang−Rhys parameters with values substantially smaller than 1 in Tables 2 and 3. A simple Franck−Condon analysis thus suggests only a small change in the Mn−O bond length upon $^2E \leftrightarrow {}^2T_2$ LF excitation.

Jahn−Teller Effects in the ^2E and $^2T_2$ LF States. In contrast to the stretching (ν) mode, coupling of the bending (δ) mode to the electronic transitions is very pronounced. This is due to Jahn−Teller (JT) effects in both the ground and excited LF states. The active mode is a bending mode with e symmetry in the parent T_d symmetry. The $^2E \leftrightarrow {}^2T_2$ LF absorption and emission spectra of MnO_4^{2-} doped into Cs_2CrO_4 and Cs_2SO_4 are very similar, and we use the formalism described in ref 8 for $Cs_2SO_4:MnO_4^{2-}$ to calculate the JT parameters for $Cs_2CrO_4:MnO_4^{2-}$.

Let us first turn to the E ⊗ e vibronic coupling in the ground state. The e vibration consists of the two components Q_X (transforming as z^2) and Q_Y (transforming as xy) shown in Figure 8. The single-mode E ⊗ e JT Hamiltonian H_{JT} requires an additional term H_{CF} representing the noncubic crystal-field (CF)

(20) Nord, A. G. *Acta Chem. Scand.* **1976**, *30*, 198.

potential and is given by

$$H = H_0 + H_{JT} + H_{CF} \tag{1}$$

with

$$\frac{H_0}{\hbar\omega_e} = \frac{1}{2}\left(-\frac{\delta^2}{\delta X^2} - \frac{\delta^2}{\delta Y^2} + X^2 + Y^2\right)\begin{pmatrix}1 & 0\\ 0 & 1\end{pmatrix} \tag{1a}$$

$$\frac{H_{JT}}{\hbar\omega_e} = \begin{pmatrix}F_E X + G_E(X^2 - Y^2) & -F_E Y + 2G_E XY\\ -F_E Y + 2G_E XY & -F_E X - G_E(X^2 - Y^2)\end{pmatrix} \tag{1b}$$

$$\frac{H_{CF}}{\hbar\omega_e} = \begin{pmatrix}S_X & -S_Y\\ -S_Y & -S_X\end{pmatrix} \tag{1c}$$

X, Y are the coordinates of the e vibration Q_X, Q_Y made dimensionless. Likewise, F_E and G_E are the linear and second-order JT coupling constants f_E and g_E, respectively, made dimensionless. S_X, S_Y are the two components of the noncubic CF potential in Cs_2CrO_4. They transform as z^2 and xy in the cubic limit and describe static distortions along Q_X and Q_Y, respectively. To restrict the number of parameters, we set S_Y to zero and packed all low-symmetry effects into the single parameter S_X. This corresponds to a slight rotation of the Q_X, Q_Y coordinate system in order to cause the displacements of the minima of the two sheets of the ground-state adiabatic potential energy surface (APS) along Q_Y to vanish.

In the case of the $^2T_2$ excited state, the $T_2 \otimes e$ JT coupling leads to an APS consisting of three equivalent parabolas in X, Y space intersecting at $X = Y = 0$ in the cubic limit. The noncubic CF potential in Cs_2CrO_4 lifts the orbital degeneracy of $^2T_2$. The $^2A'(yz)$ component (Figure 7) serves as inital state for the $^2T_2 \rightarrow {}^2E$ emission. The corresponding vibronic Hamiltonian to first order can be written as

$$\frac{H}{\hbar\omega_e} = \frac{1}{2}\left(-\frac{\delta^2}{\delta X^2} - \frac{\delta^2}{\delta Y^2} + X^2 + Y^2\right) + F_T\left(-\frac{1}{2}X + \frac{\sqrt{3}}{2}Y\right) \tag{2}$$

where F_T denotes the linear vibronic coupling constant f_T made dimensionless.

There are seven parameters required to simultaneously describe the $E \otimes e$ and $T_2 \otimes e$ JT vibronic surfaces and thus calculate the spectra. For the ground state these are F_E, G_E, and S_X (see eq 1), a constant C corresponding to the ratio of the overall intensity of emissions J and I, and $\hbar\omega_e$, the energy of the e vibration. For the excited state the parameters are $\rho = |F_T|$ and ϕ, corresponding to the magnitude and orientation of the displacement of the energy minimum of the emitting $^2A'(yz)$ ($^2T_2$) state in the X, Y space, respectively. These parameters were determined by fitting the observed vibronic levels in the emission spectrum, and their values are listed in Table 5. The dimensionless ρ was converted into ρ' in the Q_X, Q_Y space (in angstrom units) using the following relation:

$$\rho' = \frac{5.806}{\sqrt{\hbar\omega_e \mu}}\rho \tag{3}$$

where $\mu = {}^1/_3 \cdot m(O)$ is the appropriate reduced mass for the e bending mode.[21] Analogous expressions hold for the conversion of X into Q_X and Y into Q_Y, respectively.

Table 5. Jahn−Teller Parameters, Stabilization Energies, and Angular Distortions for MnO_4^{2-} in Cs_2CrO_4 and Cs_2SO_4[8] Obtained from Fits of the Experimental Emission Spectra[a]

	Cs_2CrO_4	Cs_2SO_4		Cs_2CrO_4	Cs_2SO_4
F_E	0.318	0.294	C	2.43	2.56
G_E	0.044	0.039	$E_{JT}(^2E)$, cm^{-1}	16	14
S_X	1.64	1.55	$E_{JT}(^2T_2)$, cm^{-1}	928	925
F_T	−2.39	−2.35	r_{Mn-O}, Å	1.63	1.60
ρ', Å	0.354	0.336	$\Delta\theta(\epsilon_+)$, deg	1.5	1.4
ϕ, deg	154	155	$\Delta\theta(\epsilon_-)$, deg	−1.8	−1.6
$\hbar\omega_e$, cm^{-1}	288	309	$\Delta\theta(T_2)$, deg	11.2	10.5
$\hbar\omega_e'$, cm^{-1}	325	335	$\Delta\varphi(T_2)$, deg	5.5	4.9

[a] Definitions of the symbols in the first column are given in section 4.1.1.

The JT stabilization energies E_{JT} for the ^2E and $^2T_2$ states are given by[22]

$$E_{JT}(^2E) = \frac{F_E^{\,2}}{2(1 - 2|G_E|)}\hbar\omega_e \tag{4a}$$

$$E_{JT}(^2T_2) = \frac{F_T^{\,2}}{2}\hbar\omega_e' \tag{4b}$$

where $\hbar\omega_e = 288$ cm^{-1} and $\hbar\omega_e' = 325$ cm^{-1} are the energies of the e vibration in the ^2E and $^2T_2$ states, respectively. With the fitted parameters we obtain JT stabilization energies $E_{JT}(^2E) = 16$ cm^{-1} and $E_{JT}(^2T_2) = 928$ cm^{-1} for the ^2E and $^2T_2$ states, respectively (see Table 5). The JT effect is much stronger in the $^2T_2$ state than in the ground state. This is a consequence of the different antibonding characters of the e and t_2 molecular orbitals, which are of π and $\sigma + \pi$ types, respectively. Moreover, the much stronger orbital splitting in the ground state leads to a larger quenching of the JT effect.

For MnO_4^{2-} doped into Cs_2CrO_4 and Cs_2SO_4, the situation in the ground state is very different from the linear $E \otimes e$ JT problem, for which the APS takes the form of the well-known "Mexican hat". In the present case the noncubic crystal field potential dominates the JT effect, and the ground-state APS is divided into two parabolas separated by the ^2E ground-state splitting of 960 cm^{-1}. These lower (ϵ_-) and upper (ϵ_+) sheets correspond in essence to the potentials of the electronic functions $|xy\rangle$ and $|z^2\rangle$ (see Figure 7), respectively. The contour plots of these sheets are shown in Figure 9. For ϵ_- they take the form of an ellipse, whereas for ϵ_+ the contour lines are almost circular. This provides the key to an understanding of the different sideband structures of the emissions I and J (see Figure 5). Because of the different curvatures of the potential ϵ_- along Q_X and Q_Y, the vibrational energies of the two components Q_X and Q_Y are different, leading to a splitting of the initially degenerate vibronic levels of ϵ_- and thus to the observed splitting of the sidebands of emission I. In the case of the ϵ_+ sheet, the JT effect leads to an increase of the curvatures of the potential along Q_X and Q_Y by almost similar amounts. Therefore the vibronic levels of ϵ_+ remain nearly degenerate, and the sideband splitting remains unresolved. The much larger line widths of the sidebands of emission J compared to those of origin J are probably due to this unresolved splitting. In the ^2E ground state, the minima of both the ϵ_+ and ϵ_- sheets are displaced along Q_X. These displacements ΔQ_X can be converted into angular distortions from the regular tetrahedron. For a displacement ΔQ_X along Q_X the tetrahedral O−Mn−O angles

(21) Cyvin, S. J. *Molecular Vibrations and Mean-Square Amplitudes*; Elsevier: Amsterdam, 1968.

(22) Bersuker, I. B. *The Jahn-Teller Effect and Vibronic Interactions in Modern Chemistry*; Plenum: New York, 1984.

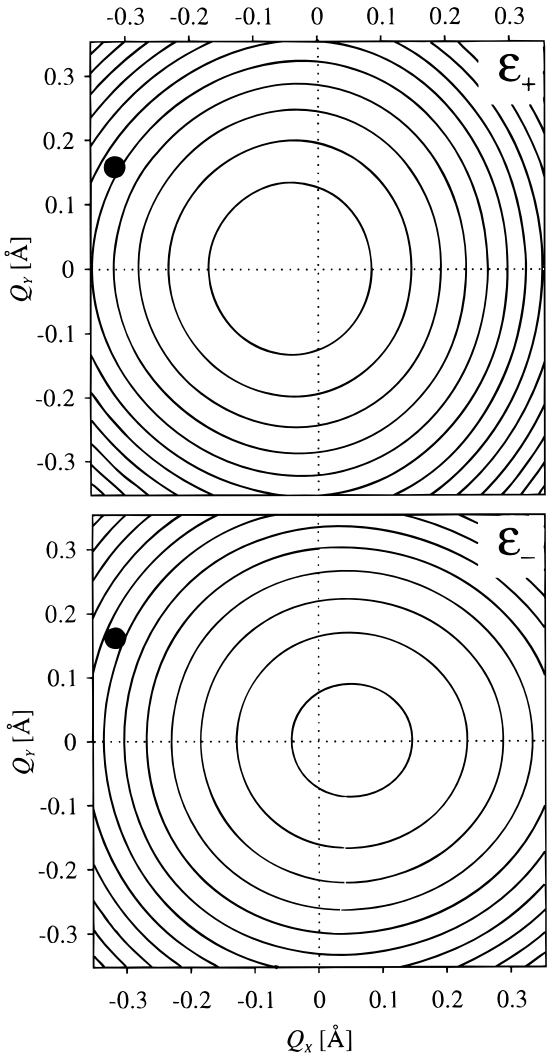

Figure 9. Contour plots of the upper (ϵ_+) and lower (ϵ_-) sheets of the adiabatic potential-energy surface for the ^{2}E ground state of MnO_4^{2-} doped into Cs_2CrO_4 as a function of the Jahn−Teller-active coordinates Q_X, Q_Y, calculated using the potential-energy terms of eq 1 and the parameters of Table 5. The points indicate the geometry of the lowest-energy excited state.

θ for the two pairs of oxygens which are intersected by z in Figure 8 change by $\Delta\theta = -(\Delta Q_X/r_{Mn-O})$, where both ΔQ_X and the Mn−O bond length r_{Mn-O} are in angstrom units. The displacements ΔQ_X lead to a compression of the MnO_4^{2-} ion along z by $\Delta\theta(\epsilon_+)$ for ϵ_+ and an elongation along z by $\Delta\theta(\epsilon_-)$ for ϵ_-, respectively (see Table 5). The black spot in Figure 9 shows the energy-minimum position in Q_X, Q_Y space of the emitting $^2A'(yz)$ ($^2T_2$) state. It is displaced along both the Q_X and Q_Y coordinates, corresponding to a compression along z by $\Delta\theta(T_2)$ and a torsional twist by $\Delta\varphi(T_2) = \Delta Q_Y/r_{Mn-O}$, respectively, where $\varphi = 90°$ for a regular tetrahedron. The large values for ρ' and ϕ (Table 5) indicate the substantial angular distortions of MnO_4^{2-} in its $^2A'(yz)$ ($^2T_2$) state due to the $T_2 \otimes e$ JT effect.

A comparison of the Cs_2CrO_4 and Cs_2SO_4 hosts shows very similar JT parameters of MnO_4^{2-} in both systems, leading to almost identical magnitudes of the JT effect in the ^{2}E and $^2T_2$ states; see Table 5. Since the energy of the e vibration $\hbar\omega_e$ is substantially lower in Cs_2CrO_4 than in Cs_2SO_4, the potentials are shallower and the angular distortions larger in Cs_2CrO_4 (Table 5).

4.1.2. $SrCrO_4$ Host Lattice. $SrCrO_4$ has a monoclinic crystal structure of the monazite type with the space group $P2_1/n$ and $\beta = 103.08°$. The MnO_4^{2-} site symmetry is C_1.[13] However, the deviations from D_2 are small, and the optical spectra can be interpreted in D_2 symmetry in a good approximation. The molecular z axis is almost parallel to the crystallographic c axis, and the x and y axes make angles of about 20° with a and b, respectively. To study the effect of the $T_d \rightarrow D_2$ distortion on the $^2E \leftrightarrow {}^2T_2$ LF transitions of MnO_4^{2-}, we performed a crystal-field analysis within the framework of the angular overlap model (AOM) using the CrO_4^{2-} host tetrahedron geometry.[13] Spin−orbit coupling was neglected because it is strongly quenched by the crystal field. From the calculated splitting pattern which is shown schematically on the left-hand side of Figure 7, it can be seen that the unpaired electron occupies the $d_{x^2-y^2}$ orbital in the ground state of MnO_4^{2-}. This gives rise to the selection rules shown by arrows in Figure 7: short-dashed, long-dashed, and solid lines correspond to x-, y-, and z-polarized transitions, respectively.

On the basis of the selection rules sketched in Figure 7, we assign the $E||c$ polarized absorption (Figure 3) and emission (Figure 5) to transition I = I (Figure 7). Equating the appropriate AOM expression with the absorption maximum at 11 272 cm^{-1} and setting e_π^O/e_σ^O equal to 0.2, we obtain e_σ^O = 11 528 cm^{-1}, which compares well with the corresponding value of 10 856 cm^{-1} for the Cs_2SO_4 host.[8] In contrast to the case of the Cs_2CrO_4 host discussed above, we were able to observe neither the x- and y-polarized absorption transitions II and III nor the z-polarized luminescence transition J predicted by Figure 7 in this host.

At first sight, the line at 10 013 cm^{-1} (labeled #) in the luminescence spectrum of Figure 5 has the appearance of a second origin. However, the following considerations show that an assignment to origin J is very unlikely: The resulting ^{2}E ground-state splitting of 290 cm^{-1} would be much smaller than the value of 567 cm^{-1} found from the AOM calculation. Furthermore, the intensity ratio of the origin line I to the line # is the same in both polarizations and no vibrational sideband corresponding to line # could be observed. We therefore assign this line to a sideband corresponding to one quantum of the t_2 bending mode of MnO_4^{2-}. In a basic aqueous solution, the frequency of this mode was found to be 332 cm^{-1}.[23]

We are therefore left with the conclusion that the intensity of the LF transition is predominantly concentrated in component I corresponding to $^2A(x^2 - y^2) \leftrightarrow {}^2B_1(xy)$ in the $SrCrO_4$ host lattice. The other formally allowed components are swamped by I in both absorption and emission. As seen in Figures 3 and 5, as well as Table 2, the coupling to the δ mode with e parent symmetry in T_d is again dominant and essentially determines the shape of both absorption and emission bands. With an $S(\nu)/S(\delta)$ ratio of about 1/8, coupling to the totally symmetric ν mode is even less important in this host than in Cs_2SO_4 and Cs_2CrO_4. We conclude that by far the most dominant vibronic coupling effect is the $T_2 \otimes e$ Jahn−Teller coupling in the excited LF state. The δ-sideband splittings clearly observable in the luminescence spectrum of Figure 5 are the result of the weaker $E \otimes e$ coupling in the ground state, similar to the situation in Cs_2CrO_4; see section 4.1.1.

4.1.3. CsBr and CsI Host Lattices. The low-temperature absorption and luminescence spectra of MnO_4^{2-}-doped CsBr and CsI lattices are characterized by their similarity and by the

(23) Gonzalez-Vilchez, F.; Griffith, W. P. *J. Chem. Soc., Dalton Trans.* **1972**, 1416.

similarity to those of pure Cs_2MnO_4. In particular, the electronic ground-state splitting is of the order of 950−960 cm^{-1} for all the three samples whereas, for $SrCrO_4$ (567 cm^{-1}) and $BaSO_4$ (∼370 cm^{-1}), it is substantially smaller. The splitting is similarly large in Cs_2SO_4 (969 cm^{-1}) and Cs_2CrO_4 (960 cm^{-1}), and in these lattices it has been ascribed to the crystal-field potential resulting from the Cs^+ ions, from which the guest MnO_4^{2-} ion is poorly shielded in the β-K_2SO_4 type structure.

Combined with the microscopic observation of microscale crystalline inclusions in the MnO_4^{2-}-doped CsBr crystals, this is a clear indication that the MnO_4^{2-} ions are not molecularly dispersed in these lattices but rather occur as microcrystals of Cs_2MnO_4. To test this hypothesis, we artificially created such "crystals" by pressing a pellet of a finely ground powder of Cs_2MnO_4-doped CsCl. The near identity of the spectroscopic properties with those of MnO_4^{2-}-doped CsBr and CsI crystals on one hand and the pure Cs_2MnO_4 on the other fully confirms the above hypothesis. CsBr and CsI in the molten state act as a flux medium for the growth of Cs_2MnO_4 crystals.

The decrease in resolution in the emission spectra (Figure 6) from CsCl:Cs_2MnO_4 to CsI:MnO_4^{2-} correlates well with the decrease of the observed size of the Cs_2MnO_4 crystallites (≤50 μm in the CsCl, ≤25 μm in the CsBr, and too small to be observable in the CsI host lattices). With decreasing size of the crystallites, the site for MnO_4^{2-} becomes more and more ill-defined, which leads to increasing inhomogeneous line broadening.

The luminescence decay behavior of MnO_4^{2-}-doped CsBr and CsI strongly supports the hypothesis that the luminescence arises from crystallites of Cs_2MnO_4. In contrast to those of all the other MnO_4^{2-}-doped crystal systems studied so far, the decays at 10 K in both of these systems are significantly faster and nonexponential. In addition, thermal quenching begins at significantly lower temperatures than that in the other host lattices; see Table 4. Since the luminescence decay behavior of pure Cs_2MnO_4 is very similar in all these respects, the observed luminescence in the CsBr and CsI lattices originates from crystallites of Cs_2MnO_4 with dimensions up to 50 μm. It is remarkable that pure Cs_2MnO_4 shows detectable luminescence up to about 160 K. Concentration quenching is usually very pronounced in undiluted compounds of the 3d metals. In the present system, energy migration to killer traps is unusually inefficient because the energy transfer step between nearest neighbors is slow. This is the result of the unusually large geometric distortion of the excited state versus the ground state along the e (δ) Jahn−Teller coordinate. This leads to the unusually large Stokes shift of approximately 3400 cm^{-1} and thus a very small spectral overlap between the emission and absorption profiles. This spectral overlap is a factor in the expression for the excitation energy transfer between MnO_4^{2-} centers in the lattice and may be the key factor for understanding the observed behavior of Cs_2MnO_4. Energy migration does occur in Cs_2MnO_4 at 10 K, and the luminescent centers are shallow traps, most likely MnO_4^{2-} centers on slightly perturbed sites. A distribution of such sites is the likely reason for the nonexponentiality of the 10 K luminescence in these systems.

Our conclusion about the nature of the chromophores and luminophores in MnO_4^{2-}-doped halides is at variance with earlier studies in which it was assumed that MnO_4^{2-} ions were substituting for halide ions in the host lattice.[10] No luminescence spectra were available in these earlier investigations, whereas the most conclusive evidence for the presence of Cs_2MnO_4 cystallites in our work is the spectral and temporal behavior of the luminescence.

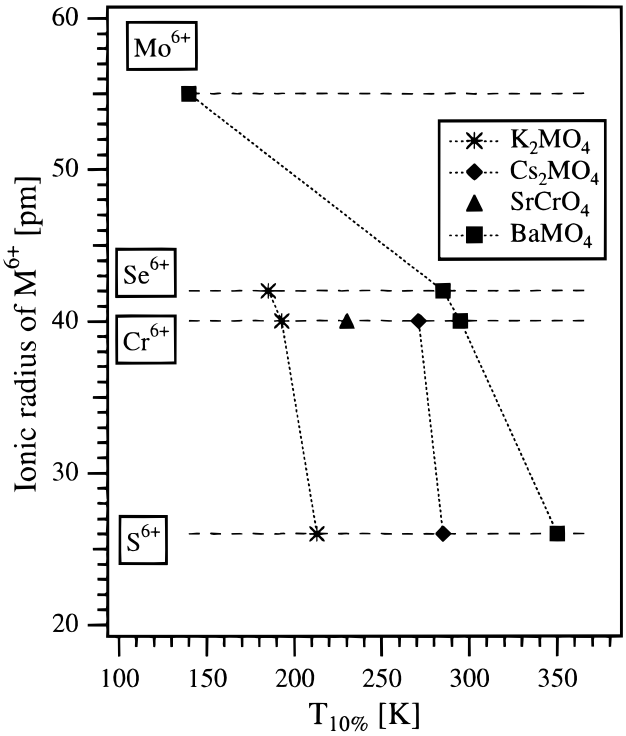

Figure 10. Temperature $T_{10\%}$ at which the luminescence intensity of MnO_4^{2-} is reduced to 10% of its 10 K value (Cs_2CrO_4 and $SrCrO_4$: 20 K) versus the ionic radius of M^{6+} for different host lattices.

4.1.4. Multiphonon Relaxation. Radiative luminescence transitions are always in competition with nonradiative processes. Concentration quenching based on energy migration to killer traps may be very efficient in undiluted systems, as discussed for Cs_2MnO_4 in the preceding section. In diluted crystals with MnO_4^{2-} concentrations considerably below 1%, these can be neglected and multiphonon relaxation is the main competitor. The seven top entries in Table 4 represent the seven host lattices for MnO_4^{2-} explored so far, and we will now interpret the observed values of τ_{obs}(10 K) and $T_{10\%}$ in terms of a simple model which has some predictive value. The definition of $T_{10\%}$, the temperature at which the luminescence intensity has dropped to 10% of its 10 K value, is an attempt to characterize and quantify the thermal quenching behavior by one number.

In all the lattices above the broken line in Table 4, both the luminescence intensity and lifetime remain approximately constant between 10 and 100 K. Both quantities then gradually decrease upon further temperature increase. For $BaSO_4$:MnO_4^{2-} we have shown that the luminescence lifetime below 100 K is purely radiative and thus the quantum efficiency is 1.[9] We assume the same to be true for the other lattices. Multiphonon relaxation processes occur at higher temperatures. The significantly different $T_{10\%}$ values in Table 4 reflect their different efficiencies. For better efficiency, we have plotted in Figure 10 the $T_{10\%}$ values for the various lattices as a function of the ionic radius of the M^{6+} ion for which Mn^{6+} substitutes. Within isomorphous lattice types, we see a clear trend of increasing $T_{10\%}$ with decreasing ionic radius of M^{6+}. Thus, for the $BaSO_4$ structure type, we have more than a doubling of $T_{10\%}$ between $BaMoO_4$[24] and $BaSO_4$, corresponding to a reduction of more than 50% of the M^{6+} radius. It is conceivable that the Mn−O distances of the guest MnO_4^{2-} ion will to some degree adapt to

(24) Crystallizes in the tetragonal scheelite structure with space group $I4_1/a$.

the host lattice. This means that the ligand field and thus the $^2E-{}^2T_2$ energy splitting will be largest in the lattices with the smallest M^{6+} radius within a given structure type. This is very nicely borne out by experiment, as shown in the last column of Table 4, listing the energies of the electronic origins *J*. These actually correspond to the smallest electronic energy gap between $^2T_2$ and ^2E. This energy gap is an important parameter for multiphonon relaxation processes. The nonradiative relaxation rate exponentially decreases with increasing number of phonons required to bridge this gap. Thus the observed trends within a given structure type in Table 4 and Figure 10 can be understood. $T_{10\%}$ can be established for host lattices not yet explored by extrapolating Figure 10 in a straightforward way.

We can also qualitatively understand the influence of the cation in the host material. This influence is significant: The $T_{10\%}$ values for the Cs_2SO_4 and Cs_2CrO_4 host lattices are about 30% higher than those for the corresponding potassium lattices. For the Cs salts, the energies of the highest energy stretching (ν) modes of MnO_4^{2-} are lower by about 3%. This is the relevant mode in the multiphonon relaxation,[25] and thus these processes are least competitive in the low phonon energy Cs and Ba hosts. $BaSO_4$:MnO_4^{2-} with a $T_{10\%}$ value of 350 K and a quantum efficiency at 300 K of 20% is the host lattice in which multiphonon relaxation is least competitive. This, together with its low solubility in water, makes this system a potential candidate for application as a NIR solid-state laser material. The very broad luminescence extending from about 900 to 1500 nm at room temperature and the established weakness of excited-state absorption in this wavelength range[26] are additional attractive features which warrant a further investigation of this material.

4.2. $^2E \rightarrow {}^2T_2$ Ligand-to-Metal Charge-Transfer Transition. The first excited LMCT electron configuration of MnO_4^{2-} is $t_1^5 e^2$; i.e., one electron is promoted from the fully occupied set of t_1 ligand orbitals to the essentially metal-centered set of e molecular orbitals. The corresponding doublet ligand-to-metal charge-transfer (LMCT) states are $^2T_2$, $^2T_2$, $^2T_1$, and $^2T_2$, of which a $^2T_2$ is lowest in energy. The origin positions of the corresponding $^2E \rightarrow {}^2T_2$ LMCT transition of MnO_4^{2-} in several host lattices are listed in Table 1. As for the ligand-field excitations, we observe a dependence of the first LMCT energy on the size of the M^{6+} ion for which Mn^{6+} substitutes within a given structure type. Thus the origin positions are higher in Cs_2SO_4 than in Cs_2CrO_4 and higher in $BaSO_4$ than in $BaSeO_4$. In the CsBr- and CsI-doped samples, the $^2E \rightarrow {}^2T_2$ LMCT origins are very similar in energy to that of Cs_2CrO_4:MnO_4^{2-}, in full support of our notion that the chromophores in these halide-doped systems are Cs_2MnO_4 crystallites with the same structure as Cs_2CrO_4.

In all the host lattices studied so far, the lowest-energy $^2E \rightarrow {}^2T_2$ LMCT band exhibits a fairly resolved vibrational progression. The Huang−Rhys parameters in Table 1 were obtained by fitting simulated band shapes to the experimental spectra of the totally symmetric stretching (ν) mode in a simple Franck−Condon analysis. Assuming harmonic potentials and equal force constants in the ground and excited states, the corresponding increase of the Mn−O equilibrium distance in the excited state is given by

$$\Delta(\mathrm{Mn-O}) = \frac{1}{2}\Delta Q_{\tilde{\nu}} = \frac{1}{2}\sqrt{\frac{S\hbar}{\pi c\tilde{\nu}\mu}} \qquad (5)$$

S and $\tilde{\nu}$ are the Huang−Rhys parameter and vibrational frequency (in cm^{-1}) for the progression in the totally symmetric stretching mode, respectively, and μ is the reduced mass which, for that mode, corresponds to the oxygen mass.[21] The Δ(Mn−O) values thus obtained for the systems listed in Table 1 range from 0.045 to 0.060 Å.

In the absorption spectra of Cs_2CrO_4:MnO_4^{2-} (see Figure 1), the observation of one and two origins in *a* and *b* polarizations, respectively, is due to an orbital splitting of the $^2T_2$ LMCT state. This polarization behavior is consistent with the C_s selection rules shown in Figure 7. In the case of $SrCrO_4$:MnO_4^{2-}, a single, predominantly $E||c$ polarized LMCT band is observed, very similar to the situation in the $^2E \rightarrow {}^2T_2$ LF absorption region.

Acknowledgment. We thank Mark J. Riley, University of Queensland, Australia, for providing the computer program for the Jahn−Teller calculation and the Swiss National Science Foundation for financial support.

IC971004G

(25) Brunold, T. C.; Güdel, H. U.; Kaminskii, A. A. *Chem. Phys. Lett.* **1997**, *271*, 327.
(26) Brunold, T. C.; Güdel, H. U.; Kück, S.; Huber, G. *J. Opt. Soc. Am. B* **1997**, *14*, 2373.